dHybridR: A Hybrid Particle-in-cell Code Including Relativistic Ion Dynamics

Colby C. Haggerty and Damiano Caprioli

Department of Astronomy and Astrophysics, University of Chicago, 5640 S Ellis Ave, Chicago, IL 60637, USA; chaggerty@uchicago.edu
Received 2019 September 10; revised 2019 November 11; accepted 2019 November 17; published 2019 December 18

Abstract

We present the first plasma simulations obtained with the code <code>dHybridR</code>, a hybrid particle-in-cell code with fluid electrons and both thermal and energetic ions that retain relativistic dynamics. <code>dHybridR</code> is constructed to study astrophysical and space-physics problems where a few energetic nonthermal particles (i.e., cosmic rays, CRs) affect the overall dynamics of a nonrelativistic plasma, such as CR-driven instabilities, collisionless shocks, magnetic reconnection, turbulence, etc. In this method paper we provide some applications to linear (resonant/nonresonant CR streaming instability) and strongly nonlinear (parallel shocks) problems that show the capabilities of the code. In particular, we provide the first self-consistent hybrid runs that show the acceleration of relativistic ions at nonrelativistic shocks; CRs develop a power law in momentum, which translates into a broken power law in energy that exhibits a steepening around the ion rest mass, as predicted by the theory of diffusive shock acceleration. We present examples of 2D <code>dHybridR</code> runs relevant for fast shocks in radio supernovae, whose evolution can be followed in real time, and 3D runs of low-Mach-number heliospheric shocks, which can be compared with in situ spacecraft observations.

Unified Astronomy Thesaurus concepts: Plasma astrophysics (1261); Shocks (2086); Cosmic rays (329); Galactic cosmic rays (567); Space plasmas (1544); Plasma physics (2089); Magnetohydrodynamical simulations (1966)

1. Introduction

Understanding the generation and dynamical effects of nonthermal high-energy particles (cosmic rays, CRs) in astrophysical plasmas has been an important question since their discovery in the early 20th century (see, e.g., Baade & Zwicky 1934; Fermi 1949; Chen & Armstrong 1975; Axford et al. 1977; Krymskii 1977; Bell 1978a, 1978b; Blandford & Ostriker 1978, for some representative seminal papers on the acceleration of Galactic CRs). CRs are ubiquitous throughout the universe and in the Galactic interstellar medium are in equipartition with the thermal plasma and the magnetic fields, despite being very few in number, about 10^{-9} times less abundant than thermal protons (e.g., Yoast-Hull et al. 2014, and references therein).

Self-consistent modeling of the nonlinear interplay between CRs, thermal plasma, and magnetic fields is a challenging problem and requires kinetic numerical approaches; moreover, such a nonlinear physics inherently spans multiple length and timescales. For instance, the gyroradius of a GeV particle is about 10^{12} cm in the μ G magnetic field typical of heliospheric and interstellar media, significantly larger than electron/ion skin depths, which are on the order of 10^5 – 10^7 cm for typical densities of about 1 cm⁻³. Accelerators can be several orders of magnitude larger: $\sim 10^9$ cm for the Earth bow shock, a fraction to a few astronomical units for interplanetary shocks, tens of parsec for Galactic supernova remnants, and even a few megaparsec for radio relics in galaxy clusters.

Fully kinetic plasma models (like particle-in-cell, hereafter PIC, or Vlasov codes) can accurately model all of the relevant physics in collisionless systems by evolving the six-dimensional phase-space distribution function of both ions and electrons (e.g., Birdsall & Langdon 1991; Bell et al. 2006; Valentini et al. 2007; Lapenta 2012; Palmroth et al. 2018). However, these fully kinetic simulations require grid sizes and time steps that resolve both the electron and ion dynamics, and because an electron is a factor of 1836 lighter than a proton, the

characteristic scales of the electron dynamics are significantly smaller than those of the ions. Having to resolve the electron scales limits the ability of these approaches to model the long-term evolution of the ions, and especially, of the CRs.

The hybrid model, which treats ions as kinetic macroparticles that satisfy the Vlasov equation with phase-space trajectories evolved by the Lorentz force equation and electrons as a fluid that keeps the system charge neutral, can bridge thermal and nonthermal regimes at the expense of the detailed kinetic electron physics. Hybrid models (see Winske & Omidi 1996; Lipatov 2002, for reviews) have been used to study many different plasma problems, including shocks (e.g., Winske 1985; Quest 1988; Burgess 1989; Giacalone et al. 1992; Giacalone 2004; Gargaté & Spitkovsky 2012; Burgess & Scholer 2013; Caprioli 2015; Burgess et al. 2016), turbulence (e.g., Karimabadi et al. 2014; Matthaeus et al. 2015; Pecora et al. 2018; Arzamasskiy et al. 2019), and magnetic reconnection (e.g., Mandt et al. 1994; Shay et al. 2001; Le et al. 2009).

An implicit assumption of the hybrid model, however, is that the speed of light is taken to be infinitely high, in order to neglect Maxwell's correction in the Ampère law (see Section 2 for more details), which forces the ion dynamics to be nonrelativistic. This restriction is significant for modeling the physics of CRs and may raise concerns when simulations are compared with observations.

Alternative approaches have used a kinetic description of CRs, while treating the thermal population as a magnetohydrodynamical (MHD) fluid (e.g., Zachary & Cohen 1986; Lucek & Bell 2000; Bai et al. 2015; Mignone et al. 2018; van Marle et al. 2018; Dubois et al. 2019). While these MHD-PIC simulations can capture some CR physics, the gap between thermal and energetic particles requires the injection of CRs in the system to be externally prescribed, rather than modeled from first principles.

In this work we present the first—to our knowledge—hybrid code that includes relativistic ion dynamics, dHybridR, which is built upon the massively parallel Newtonian code *dHybrid*

(Gargaté et al. 2007). In Section 2 we outline the basics of the code, and we argue that the set of systems with both thermal and CR populations can be modeled in this way without violating any of the hybrid approximations. In Section 3 we compare <code>dHybridR</code> simulations of CR streaming instabilities with linear theory predictions and show that the physics of CRs and thermal plasma interaction are being correctly modeled. In Section 4 we investigate the acceleration of CRs in parallel shocks and the lack thereof in oblique shocks. Finally, in Section 5, we show a 3D simulation of an oblique low-Machnumber shock with parameters comparable to the Earth's bow shock, which exhibits features consistent with very recent in situ observations (Johlander et al. 2016, 2018).

2. Hybrid and dHybridR

The hybrid model for simulating collisionless plasma physics is fundamentally a Monte Carlo approach to solving the Vlasov–Maxwell system of equations:

$$\frac{\partial f_s}{\partial t} + \mathbf{v} \cdot \mathbf{\nabla} + \frac{q_s}{m_s} \left(\mathbf{E} + \frac{\mathbf{v}}{c} \times \mathbf{B} \right) \cdot \mathbf{\nabla}_{\!v} f = 0 \tag{1}$$

$$\frac{\partial \mathbf{B}}{\partial t} = -c \mathbf{\nabla} \times \mathbf{E} \tag{2}$$

$$\frac{\partial \boldsymbol{E}}{\partial t} = c\boldsymbol{\nabla} \times \boldsymbol{B} - 4\pi \boldsymbol{J} \tag{3}$$

$$\nabla \cdot \mathbf{B} = 0 \tag{4}$$

$$\nabla \cdot \boldsymbol{E} = \sum_{s} q_{s} n_{s},\tag{5}$$

where E and B are the electric and magnetic fields, $f_s(x, v, t)$ is the phase-space distribution function for a given species s of particles with charge q_s and mass m_s , $n_s \equiv \int f_s d^3 v$ is the number density of species s, and $J \equiv \sum_s q_s n_s V_s$ is the total current, where $V_s \equiv \int v f_s d^3 v / n_s$ is the bulk velocity of each species. In this work only electron-proton plasmas are considered, but ions with arbitrary mass and charge can be easily accounted for (e.g., Caprioli et al. 2017).

The motivation of the hybrid model is to simulate kinetic ion dynamics (i.e., Equation (1)) on larger length and timescales at the expense of kinetically modeling electron dynamics. In practice this is done by assuming that the electron mass is negligibly low compared to the ion mass. In this way, electrons are treated as a massless charge-neutralizing fluid that enforces quasi-neutrality in a system. This corresponds to $n_i = n_e$ and hence to $\nabla \cdot E = 0$ (Equation (5)) and $J = en_i(V_i - V_e)$.

The evolution of the ions in time is described by Equation (1). In practice this is done by approximating the ion distribution function with a large number of macroparticles whose motion in phase space is determined by the Lorentz force. For a given set of electromagnetic fields, the macroparticle position and velocity can be advanced in time. The updated positions and velocities can be interpolated onto a grid and return a fluid density and bulk flow; note that because the electrons are taken to be massless, they do not contribute to the bulk flow.

The electric field, E, is determined by multiplying the Vlasov equation for the electrons (Equation (1)) by $m_e v$ and

integrating it over all of velocity space, which yields

$$m_e n_e \left(\frac{\partial}{\partial t} - V_e \cdot \nabla\right) V_e = -\nabla P_e - e n_e E - \frac{e n_e V_e}{c} \times B.$$
 (6)

Here we introduced the (isotropic) electron pressure P_e , which encompasses higher order moments of the electron distribution function. Reapplying the assumption that $n_i = n_e$ in the limit $m_e \ll m_i$, we derive an effective Ohm's law for the electric field.

$$\boldsymbol{E} = -\frac{\mathbf{V}_e}{c} \times \boldsymbol{B} - \frac{1}{en} \nabla P_e \tag{7}$$

$$= -\frac{\mathbf{V}_i}{c} \times \mathbf{B} + \frac{\mathbf{J}}{enc} \times \mathbf{B} - \frac{1}{en} \nabla P_e. \tag{8}$$

The next assumption required for the hybrid model is to neglect the displacement current in Ampère's law (i.e., the time derivative of the electric field) such that $\nabla \times \mathbf{B} = \frac{4\pi}{c}\mathbf{J}$; this usually referred to as the radiation-free limit, or the Darwin approximation. This assumption is often equated with taking the speed of light to be much higher than any other velocity in the system; however, we show below that it may hold even when a small number of relativistic particles are present. Ultimately, omitting this term from the hybrid model neglects the role of light waves. Finally, the electron pressure is prescribed by an equation of state, often taken as isotropic and polytropic. This electric field can then be used in Faraday's law to update the magnetic field and thus yields a closed set of equations describing the evolution of the systems.

While the behavior of the ions is fully detailed in the hybrid model, the physical description and evolution of the electrons is less well defined. This is evident in choosing the most physically appropriate value of $\gamma_{\rm eff}$ for a polytropic electron equation of state, $P_e \propto n^{\gamma_{\rm eff}}.$ It could be argued that the electrons should be adiabatic and so $\gamma_{\rm eff} = 5/3$. However, if the adiabatic description is used in shocks with a large Mach number, electrons cannot increase their entropy at the shock and the downstream electron pressure may end up being orders of magnitude lower than the ion pressure. When we assert that the electron and ion downstream pressure should be in equipartition, the Rankine-Hugoniot (RH) jump condition may be used to calculate $\gamma_{\rm eff}$ (see the appendix of Caprioli et al. 2018, for more details). More complicated anisotropic prescriptions may be needed for magnetic reconnection (e.g., Le et al. 2009). In this work we use the equipartition equation of state for shock simulations and the adiabatic equation of state for CR streaming simulations.

Along with the disparate length and timescales, plasma systems can also span multiple scales in velocity space, ranging from thermal particles that make up the bulk of the plasma to CRs with kinetic energies orders of magnitude higher than their rest mass. An implicit assumption of the Darwin model is that the bulk velocities of the system are low relative to the speed of light, and because of this, hybrid codes have traditionally not included relativistic effects for the macroparticle ions. However, because this approximation is based on bulk speeds being low relative to the speed of light, even plasma systems with a nonrelativistic background and a small number of relativistic particles (or CRs) can be modeled in this limit. This can be seen from a scaling argument of Ampère's law with Maxwell's

correction.

$$\nabla \times \mathbf{B} = \frac{4\pi}{c} \mathbf{J} + \frac{1}{c} \frac{\partial \mathbf{E}}{\partial t} \rightarrow \frac{B}{\lambda} : \frac{4\pi J}{c} : \frac{E}{c\tau}, \tag{9}$$

where derivatives have been replaced by λ and τ , which correspond to characteristic length and timescales of the systems we are interested in studying, and the colon (:) denotes an order-of-magnitude comparison. We can see from the scaling of Faraday's law that $E/B \sim V/c$, where $V = \lambda/\tau$ is the characteristic velocity of the system. Using this and that $J \sim enV$, we can simplify our scaling equation to

1:
$$\frac{\lambda}{d_i} \frac{V}{v_{\rm A}}$$
: $\left(\frac{V}{c}\right)^2$, (10)

where $d_i = c/\omega_{\rm pi} = \sqrt{c^2m_i/4\pi ne^2}$ is the ion inertial length (skin depth) and $v_{\rm A} = B/\sqrt{4\pi m_i n}$ is the Alfvén speed. Neglecting the displacement current is no longer appropriate when the third term becomes comparable to the other two, and so we find that this approximation is good as long as

$$\left(\frac{V}{c}\right)^2 \ll 1$$
, and $\frac{Vv_{\rm A}}{c^2} \ll 1$, (11)

where we used 1 for λ/d_i , which is the strictest value that can be used for hybrid simulations. The systems that we aim to study are composed of a background ion thermal population with number density n_i , characteristic velocity $V_{\rm bkg} \ll c$, and a high-energy CR population with $n_{\rm cr} \ll n_i$ and $v_{\rm cr} \sim c$. The composite background + CR population bulk flow speed can be estimated as

$$\frac{V}{c} = \frac{n_i V_{\text{bkg}} + n_{\text{cr}} c}{c(n_i + n_{\text{cr}})} \approx \frac{V_{\text{bkg}}}{c} + \frac{n_{\text{cr}}}{n_i}$$
(12)

.From Equations (11) and (12), we find three conditions that the systems must meet for this approximation to be valid:

- 1. $V_{\rm bkg} \ll c$, i.e., bulk flows cannot be relativistic;
- 2. $n_{cr} \ll n_{n_i}$, i.e., the CR number density must be negligible relative to the gas number density;
- 3. $v_A \ll c$, i.e., the magnetic field energy density must be much lower than the rest-mass energy density.

The last condition is derived by taking the bulk flow velocity to be Alfvénic; note that $B/\sqrt{4\pi m_i n}$ can even exceed c, in which case the dispersion relation for an Alfvén wave needs to be modified by including the displacement current term, thus violating one of the previously outlined assumptions for hybrid (Krall & Trivelpiece 1973). These conditions are satisfied for many systems in space and astrophysical plasmas where CR acceleration, transport, and scattering are important.

To study these types of problems, we have developed dHybridR, a hybrid simulation code that retains the fully relativistic ion dynamics. dHybridR is a generalization of the *dHybrid* code (Gargaté et al. 2007), where the relativistic Lorentz force is used for the ion macroparticle evolution, i.e.,

$$m_i \frac{d\gamma \mathbf{v}}{dt} = q\mathbf{E} + \frac{q\mathbf{v}}{c} \times \mathbf{B},\tag{13}$$

where γ is the Lorentz factor of a given macroparticle and given by $\gamma = 1/\sqrt{1 - (v/c)^2}$. This is implemented in the code

using the well-documented relativistic Boris algorithm (see Birdsall & Langdon 1991, for details).

The equations that govern both the electromagnetic fields and the particle dynamics are normalized to arbitrary magnetic field, B_0 , and number density, n_0 . Lengths are scaled to the ion inertial length based on this density, $L_0 \equiv d_{i0} = c/\omega_{\mathrm{pi0}}$, and time to the inverse ion gyrofrequency based on this magnetic field, $t_0 \equiv \Omega_{ci0}^{-1} = \frac{cm_i}{eB_0}$. Velocities are normalized to the ratio of the length and time normalizations, and so a velocity of unity corresponds to the Alfvén speed in the reference magnetic field and density, $v_0 \equiv L_0/t_0 = B_0/\sqrt{4\pi m_i n_0}$. Electric fields are normalized to $B_0 v_0 / c$ and temperatures and energies to $m_i v_0^2$. Throughout this work, simulations are initialized such that the unshocked/background plasma has a magnetic field, density, and ion/electron temperature of unity, and so the simulation units are effectively normalized to the background/upstream plasma parameters, i.e., $v_0 = v_A = v_{th}$ and $d_{i0} = d_i = c/\omega_{pi} = r_{g,th}$, the gyroradius of the thermal ions. By normalizing the discretized equations in this way, the speed of light only appears as the ratio c/v_0 and then only occurs in the Lorentz factor, $\gamma(v) =$ $1/\sqrt{1-(v/v_A)^2(v_A/c)^2}$, in the Lorentz force equation.

The magnetic field is evolved using a two-step Lax-Wendroff scheme that is second-order accurate in space and time (Hockney & Eastwood 1988; Birdsall & Langdon 1991). Further details about the nonrelativistic implementation of dHybridR are described in Gargaté et al. (2007). The grid size is selected to resolve both the ion inertial length and the thermal ion gyroradius. The time step is chosen so that the fastest ions in the system do not move more than a single grid space in a time step, i.e., $\Delta t \leqslant (v_{\rm A}/v_{\rm max})\Delta x$ in code units. For systems with relativistic ions, $v_{\rm max} \approx c$, and so the time step is $\Delta t \leqslant \Delta x v_{\rm A}/c$.

The remainder of this paper is dedicated to the demonstration and validation of dHybridR simulating CR generation and transport for selected plasma systems, in which a small number of highly energetic ions affects the dynamics. We examine the nonresonant streaming instability (commonly referred to as the Bell instability), the resonant streaming instability, and different regimes of collisionless shocks.

In particular, we study the transition from nonrelativistic to relativistic CR energies in fast nonrelativistic shocks; because the required time step is inversely proportional to c/v_A , we initially focus on shock environments where v_A is rather large, such as radio supernovae, where $V_{\rm sh} \sim 0.1c$, $B_0 \sim 0.1$ G and $n_0 \sim 10^3 \, {\rm cm}^{-1}$ at the peak of the synchrotron emission (e.g., Chevalier & Fransson 2006). These parameters correspond to Alfvénic mach numbers $M_A \equiv V_{\rm sh}/v_{\rm A} \sim 10$ and $c/v_{\rm A} \sim 100$. Then, we show simulations of lower Mach number shocks, which are more applicable to heliospheric systems, such as planetary bow shocks and interplanetary shocks triggered by coronal mass ejections, where plasma speeds vary between several hundreds to thousands of km s⁻¹, corresponding to Mach numbers ranging from 1 to 10 and $c/v_A \gtrsim 10^4$ (Sheeley et al. 1985; Cane & Richardson 2003). Despite the limited spatial extent of these heliospheric systems, transrelativistic and even relativistic particles can be produced in these environments as well (e.g., Reames 1999; Tylka et al. 2005; Reames 2013; Desai et al. 2016; Wilson et al. 2016).

There are numerous astrophysical systems where $c/v_{\rm A}$ and $c/v_{\rm sh}$ are considerably larger than the simulations presented in this work; however, as long as there is a clear separation of scales between the thermal/Alfvénic speed, the speed of the

shock, and the speed of light, the underlying physics can be studied fruitfully. This idea implies that the physical results from these simulations, and dHybridR in general, are potentially applicable to many different astrophysical systems.

3. Resonant and Nonresonant Streaming Instability

To verify that dHybridR correctly simulates the physics relevant to systems with CRs, we present two simulations of the CR-driven streaming instability. This occurs when a population of low-density energetic CRs drift relative to a thermal population, driving the amplification of magnetic fluctuations perpendicular to the mean field. The characteristics of the instability are controlled by the CR current density: in the weak current limit, CRs trigger the growth of modes that are gyroresonant with themselves (resonant streaming instability; e.g., Kulsrud & Pearce 1969; Skilling 1975; Bell 1978a; Zweibel 2003). In the strong current limit, instead, the return current in background electrons that is needed to enforce charge neutrality drives modes with wavelengths shorter than the CR gyroradius (nonresonant or Bell instability; e.g., Bell 2004; Weidl et al. 2019).

The kinetic theory of these instabilities and the transition between the two has been detailed, e.g., by Amato & Blasi (2009) for a CR distribution $\propto p^{-4}$ in momentum. In this case, the boundary between the two regimes is defined by the parameter (see Amato & Blasi 2009)

$$\bar{\sigma} \equiv \frac{4\pi}{c} \frac{r_L}{B} J_{\rm cr} = \frac{n_{\rm cr}}{n_i} \frac{p_{\rm min} \, v_d}{m_i \, v_{\rm A}^2},\tag{14}$$

where r_L is the gyroradius of the particles with the minimum momentum in the CR distribution, p_{\min} , and $J_{\text{cr}} = en_{\text{cr}}v_d$ is the CR current, defined by the CR number density n_{cr} and their drift velocity v_d . For $\bar{\sigma} \gg 1$ the nonresonant mode grows faster than the resonant one, while for $\bar{\sigma} \ll 1$, they grow at the same rate (Bell 2004; Amato & Blasi 2009). In the resonant regime, because CRs have a velocity spread much higher than the drift velocity, both right- and left-handed magnetic fluctuations are driven, while in the nonresonant case, only electron-driven right-handed modes are amplified.

We set up dHybridR simulations of the CR streaming instabilities with different $n_{\rm CR} \propto \bar{\sigma}$ and test both the strong and the weak current regimes. This allows us to probe the nontrivial coupling between CRs, magnetic fields, and thermal background plasma both in a MHD-like (nonresonant) and a purely kinetic (resonant) scenario.

We consider two simulations in periodic domains of size $[L_x, L_y] = [10^4, 5]d_i$ with a uniform magnetic field $\mathbf{B} = B_0\mathbf{x}$ and a stationary background population of protons with thermal speed equal to v_A . Superimposed on the background population is a lower density CR population with a power-law distribution in momentum space $f(p) \propto p^{-4}$ extending from $p_{\min}/m_i c = 1$ to $p_{\max}/m_i c = 10^4$, which is isotropic in a frame moving with a drift velocity $v_d = 10v_A$. The box transverse size makes the simulations effectively 2D for the thermal background, i.e., it is larger than the gyroradius of thermal ions, but actually 1D in terms of the CR length scales. In both simulations, the speed of light is set to be $c = 100v_A$ and there are two grid cells per d_i ; with 225 and 100 macroparticles per cell used for the background and CR populations, respectively. The CR number density relative to the background population is adjusted to

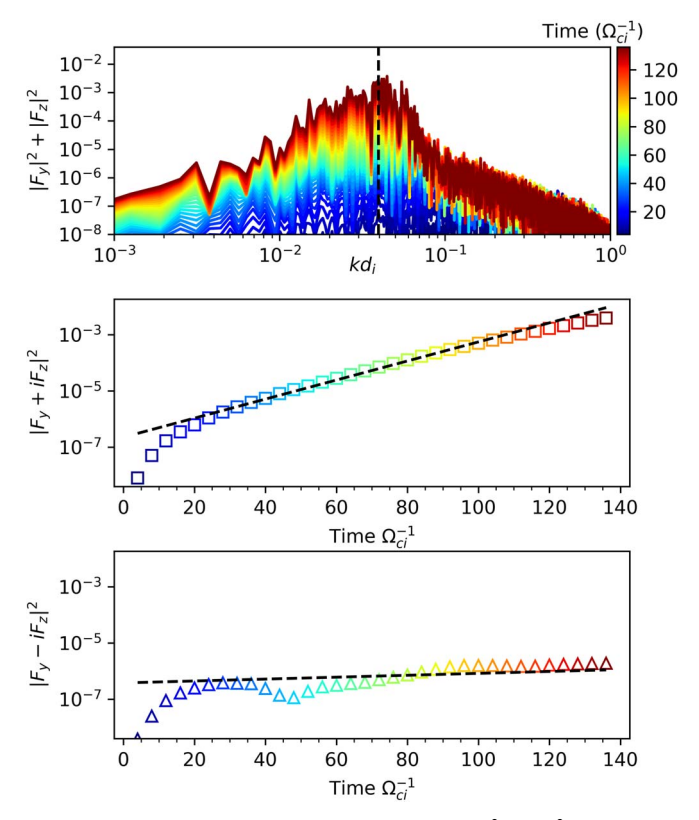


Figure 1. Perpendicular magnetic energy spectrum, $|F_y|^2 + |F_z|^2$, as a function of wave number k and time for a 1D simulation of the nonresonant streaming instability. Top panel: spectrum as a function of kd_i , where each color corresponds to a different time in the simulation; the vertical black dashed line corresponds to the k_{max} predicted by the linear theory (Equation (15)). Middle and bottom panels: magnetic power in both right-handed $(|F_+|^2 = |F_x + iF_z|^2)$ and left-handed $(|F_-|^2 = |F_x - iF_z|^2)$ modes as a function of time; the dashed lines show the growth rates predicted by the linear theory (Equation (28) of Amato & Blasi 2009).

trigger either the nonresonant $(n_{\rm cr}/n_i=10^{-2})$ or the resonant $(n_{\rm cr}/n_i=10^{-4})$ instability (Bell 2004; Amato & Blasi 2009).

Each simulation is initialized with a mean magnetic field and no electric fields. However, because of numerical noise inherent to the finite sampling of the ion distribution, there are initially density and bulk flow fluctuations. These fluctuations generate electric fields through Ohm's law (Equation (8)), which produces perpendicular magnetic perturbations that act as seeds for the unstable modes. The amplitude of this noise is controlled by the number of macroparticles per cell, and for the simulations presented in this work, the noise floor is on the order of $\langle B_{\perp}^2 \rangle_{
m noise} \sim 10^{-4} B_0^2$. From Parseval's theorem and our normalization of F, $\langle B_{\perp}^2 \rangle / B_0^2 \sim 10^{-4}$ corresponds to $\langle F_{\perp} \rangle \sim 10^{-8}$, which is consistent with the earliest times (dark blue lines) in the top panels of Figures 1 and 2. Changing the number of particles per cell alters the initial noise and changes the time that it takes to achieve saturation, but does not affect either the wavelength or the growth rate of the fastest growing modes.

For the nonresonant (or Bell) regime, the fastest growing mode is right-handed (hereafter k_{max}^+), and its corresponding growth rate, γ_{max}^+ , reads (Bell 2004)

$$\frac{\gamma_{\text{max}}^{+}}{\Omega_{\text{ci}}} = k_{\text{max}}^{+} d_{i} = \frac{1}{2} \frac{n_{\text{cr}}}{n_{i}} \frac{v_{d}}{v_{\text{A}}}.$$
 (15)

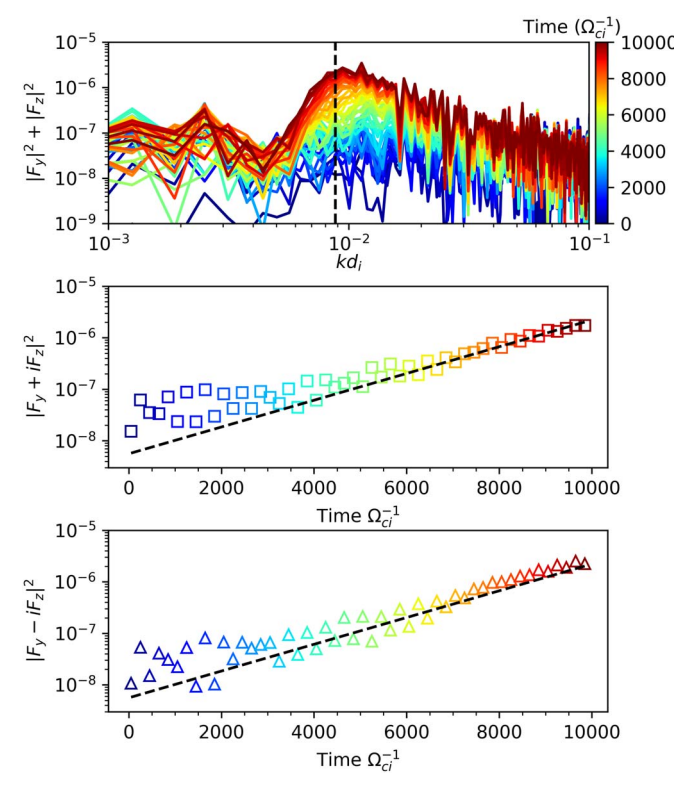


Figure 2. As in Figure 1 for a 1D simulation of the resonant streaming instability. The theoretical expectations are from Equation (16).

Instead, in the resonant regime, the fastest growing modes have no preferential helicity, and their wave numbers and growth rate read

$$k_{\text{max}}^{\pm} d_i = \frac{m_i v_{\text{A}}}{p_0}; \qquad \frac{\gamma_{\text{max}}^{\pm}}{\Omega_{\text{ci}}} \approx \frac{\pi}{8} \frac{n_{\text{cr}}}{n_i} \frac{v_d}{v_{\text{A}}},$$
 (16)

where the \pm superscripts refer to the right- and left-handed modes, respectively; Equation (16) is calculated by Taylor-expanding Equation (28) in Amato & Blasi (2009) in terms of the small parameter $n_{\rm cr} v_d p_0/(n_i m_i v_{\rm A}^2)$ and keeping only the linear term. Note that in the derivation of the dispersion relation in Amato & Blasi (2009), the drift speed is assumed to be much higher than the Alfvén speed, and so the growth rate depends on $v_D/v_{\rm A}$, rather than $v_D/v_{\rm A}-1$, as found in Kulsrud & Cesarsky (1971) and Zweibel (2003); for the parameters of the simulations presented here, this is a correction of only $\sim 10\%$.

To compare these predictions with the simulations, we introduce $F_i = \text{FFT}[B_i]/N$ for i = y, z, where FFT is the discreet fast Fourier transform calculated along the x direction and N is the number of grid points in the x direction. The magnetic power spectrum $|F_y|^2 + |F_z|^2$ is plotted in the first panels of Figures 1 and 2 for the nonresonant and resonant cases, respectively. In both figures the color corresponds to different times in the simulation and the black dashed line shows k_{max} predicted by Equations (15) and (16). There is good agreement between theory and simulation for the location of the fastest growing modes.

The second and third panels of Figures 1 and 2 show the value of the magnetic power in right-handed ($|F_+|^2 = |F_y + iF_z|^2$) and left-handed ($|F_-|^2 = |F_y - iF_z|^2$) modes as a function of time for the value of k_{max} denoted by the black dashed line in the first

panel. The magnetic energy is expected to increase exponentially in time as $|F_{\pm}|^2 \propto e^{2\gamma_{\max}^{\pm} t}$, and the black dashed line corresponds to the $2\gamma_{\max}$ given by Equations (15) and (16); there is a general agreement between theory and simulations in both the nonresonant and resonant cases. Note that the black dashed line in the bottom panel of Figure 1 is calculated using Equation (28) in Amato & Blasi (2009).

It is worth noting the differences in the time and length scales of the two instabilities we simulated. The resonant instability stems from a gyroresonant interaction with the CR population (e.g., Kulsrud & Pearce 1969) and amplifies magnetic fluctuations on scales comparable to the CR gyroradius.

Note that because $\bar{\sigma} \ll 1$ for the resonant instability, the growth rates are low compared to the cyclotron frequency of the background population (Equation (16)); but dHybridR can accurately capture this phenomenon over more than 10^4 cyclotron times (about 4×10^6 time steps).

Recent works have tackled the study of the nonresonant instability with PIC and hybrid simulations (e.g., Ohira et al. 2009; Riquelme & Spitkovsky 2009; Gargaté et al. 2010) and of the resonant instability with PIC and PIC-MHD simulations (e.g., Bai et al. 2019; Holcomb & Spitkovsky 2019; Weidl et al. 2019); these studies have generally found results consistent with theory for the fasting growing mode and corresponding growth rate for the linear phase. Nevertheless, the saturation of the CR streaming instability is a complex and nonlinear physical phenomenon that is not yet completely understood. A detailed examination of the properties of the two CR streaming instabilities using dHybridR, as well as a more thorough comparison with previous works, is in preparation (see Haggerty et al. 2019; Zacharegkas et al. 2019, for preliminary results). The agreement between simulations and the linear theory verifies that dHybridR can accurately model the physical coupling of the thermal background plasma and a drifting CR population for quasi-linear problems, both in the strong and week current regimes.

4. Nonrelativistic Shocks

4.1. Setup and Simulation Parameters

Shock simulations were performed with dHybridR following the setup described in Gargaté & Spitkovsky (2012). The simulations are performed in 2.5D (2D in real space, and 3D in momentum space) on a regular Cartesian grid, with periodic boundary conditions in the y direction (transverse to the shock), open on the right boundary (+x direction or normal and upstream of the shock), and a conducting reflecting wall on the left boundary (-x direction and downstream of the shock). The derivative along x of E_x , B_y , and B_z through the left boundary is zero, while $E_y = E_z = 0$ and $B_x = B_x(t = 0)$ in the wall. The shock is formed by initializing the plasma with a bulk flow in the -x direction; the plasma closest to the left wall is reflected and begins streaming in the +x direction. This configuration is unstable, and within ${\sim}10\Omega_{ci}^{-1},$ a shock forms and travels upstream. Across the shock, fluid quantities satisfy the RH jump conditions. For the simulations in this study, the initial/ upstream magnetic field and density are set to unity and the initial magnetic field points in the first quadrant of the x, y plane, the shock angle is measured relative to the positive x direction (normal to the shock) $\vartheta_{\rm Bn}$ (e.g., for a parallel shock ${\bf B}=B_0\hat{\bf x}$ and $\vartheta_{\rm Bn}=0$). The initial ion thermal velocity is equal to the upstream Alfvén speed and the electron temperature is equal to

the ion temperature ($T_0 = T_i = T_e$). Following previous hybrid shock simulations (e.g., Gargaté & Spitkovsky 2012; Caprioli & Spitkovsky 2014a), a polytropic index for the electron equation of state is selected so that the downstream electron thermal energy will be half of the upstream kinetic energy in the shock frame (also see Caprioli et al. 2018, for more details).

Shocks are parameterized by their Alfvénic and sonic Mach numbers, $M_{\rm A} = v_{\rm sh}/v_{\rm A}$ and $M_s = v_{\rm sh}/v_s = v_{\rm sh}/\sqrt{2\gamma k_B T_0/m_i}$, where $v_{\rm sh}$ is the upstream velocity in the laboratory/simulation frame (i.e., in the frame where the downstream medium is at rest). The choice of temperature in these simulations links the two Mach numbers, $M_{\rm A} = \sqrt{10/3}\,M_s$, and in this work, we reference the Mach number as simply $M \equiv M_{\rm A} \simeq M_s$. We use two grid cells per d_i and four particles per cell. For a parallel shock simulation, the time step is set by the speed of light, as discussed in Section 2, but for quasi-perpendicular shocks, where particles do not undergo diffusive shock acceleration (DSA), the maximum velocity is much lower than the speed of light $(v_{\rm max} \sim 3v_{\rm sh})$, and the time step is chosen accordingly.

Simulations were run for thousands of cyclotron times to model the CRs transition from nonrelativistic to relativistic energies. The largest and longest run of these simulations is shown in Figure 3 at the end of the simulation, which shows various plasma/fluid quantities around the shock. For this run we used M=20, $c=200V_{\rm A0}$, and $[L_x,L_y]=[8\times10^5,200]d_{i0}$. The speed of light limiting the fastest speed in our simulation allowed us to run unprecedentedly long hybrid simulations of nonrelativistic shocks, up to $\sim\!6000\Omega_{\rm ci}^{-1}$ before the highest energy CRs began to escape from the box.

4.2. Momentum and Energy

Consistent with results from previous nonrelativistic hybrid simulations of parallel shocks (e.g., Giacalone et al. 1997; Burgess et al. 2012; Caprioli & Spitkovsky 2014a, 2014b, 2014c), we find that thermal ions can be spontaneously energized into an extended power-law distribution. Figure 4 shows the post-shock distribution function as a function of both the ion velocity normalized to c (first panel) and the ion momentum normalized $m_{\rm ic}$ (second panel). The majority of ions are thermally heated by the shock, forming the Gaussian peak around $p/m_i \sim v \sim 0.1c$; the black dashed lines correspond to a Gaussian with temperature reduced by 20% with respect to the one predicted by the RH conditions for a mono-atomic ideal gas. The deviation form the prediction is consistent with the amount of energy (about 10%-20% of the shock ram energy) that is channeled in the nonthermal power-law distribution that develops beyond $v \sim 0.2c$, whose extent increases with time (color code). The velocity spectra are cut off at $v \leq c$, as expected, but the momentum continues to extend with the same slope beyond $p \gtrsim m_i c$. The distributions shown in Figure 4 are multiplied by v^{-4} and p^{-4} . The very reason why the spectrum looks slightly steeper than p^{-4} has profound physical reasons that will be discussed in a forthcoming paper (see Caprioli & Haggerty 2019, for a preliminary discussions).

While the momentum spectra show a nearly constant powerlaw slope, the energy spectrum should have different slopes in the nonrelativistic and relativistic regimes. The energy distribution is linked to the momentum distribution through the conservation of the phase-space volume: $f(E) = 4\pi p^2 f(p) dp/dE$. In the nonrelativistic regime, $E \propto p^2$, and so for a momentum power-law index of q, the energy distribution should go as $f(E) \propto$ $E^{(1-q)/2}$, i.e., $E^{-1.5}$ for q = 4. In the relativistic regime, $E \propto p$, and thus the kinetic energy distribution should scale as $f(E) \propto E^{2-q}$, i.e., the canonical E^{-2} for q=4.

The energy spectrum for our benchmark simulation is shown in Figure 5, where the spectrum is multiplied by $E^{1.5}$ in the top panel and E^2 in the bottom panel in an attempt to emphasize the agreement with the expected slopes in both the nonrelativistic and the relativistic regimes. In this run some particles became relativistic, with $\gamma \gtrsim 5$, but running such a large simulation long enough for the power-law tail to extend beyond $\sim 10m_ic^2$ is computationally impractical. Thus, in order to see the transition in the energy power-law slope more clearly, we performed a simulation with a lower speed of light relative to the shock velocity and Alfvén speed (Run B in Table 1); the reduced separation of scales allows us to investigate the transrelativistic regime more easily. Figure 6 shows the momentum and energy distribution for Run B at $t = 2000\Omega_{ci}^{-1}$ (top and bottom panels, respectively). In the first panel the distribution is fit with to a power law $\propto p^{-4}$ multiplied by an exponential cutoff at $p_{\text{max}} = 9m_i c$. The bottom panel shows the energy distribution, multiplied by E^2 ; the black and red dashed lines correspond to the relativistic and classical power-law predictions based on the fit curve from the top panel. In essence, the black line shows the shape of the distribution if $E = m_i c^2 (\sqrt{p^2/c^2 + 1} - 1)$ and the red line for $E = p^2/2m_i$. In the nonrelativistic regime, both the black and red predictions agree well with the measured spectrum; as the distribution extends into the relativistic regime $(E \gtrsim 2m_i c)$, however, there is a clear steepening of the slope to -2, followed by the exponential cutoff, which agrees well with the black line prediction. The classical prediction (red line), however, continues to increase for nearly an order of magnitude in energy beyond the actual energy cutoff.

This analysis shows, for the first time in hybrid simulations, how nonrelativistic shocks can accelerate particles to ultrarelativistic energies (with Lorentz factors up to $\gamma \gtrsim 20$ in our case), also confirming that DSA produces power laws in momentum space across the nonrelativistic and relativistic regimes. These results are consistent with those obtained for both electrons and ions in 1D full-PIC simulations of nonrelativistic shocks (Park et al. 2015) and for electrons in full-PIC simulations of transrelativistic shocks (Crumley et al. 2019).

One important astrophysical application that stems from these preliminary runs is relevant for young supernovae (SNe). When we consider the typical values for the magnetic field inferred in SN Ib and SN Ic with Wolf–Rayet star progenitors (Chevalier & Fransson 2006), the inverse cyclotron time $\Omega_{\rm ci}^{-1}$ would be on the order of milliseconds. Both the A and B runs have $M_{\rm A}$ and $c/v_{\rm A}$ typical of these systems, and so physically, these simulations are modeling a few seconds of fast radio SNe. Notably, in these simulations, thermal protons are accelerated to multi-GeV energies in a matter of seconds, which has implications for the generation of γ -rays and neutrinos, as discussed below.

4.3. Rate of Maximum Energy Increase

An important question regarding DSA is the maximum energy, $E_{\rm max}(t)$, of the particles produced by a shock with a given speed and magnetic field in a finite amount of time (e.g., Lagage & Cesarsky 1983; O'C. Drury 1983; Blasi et al. 2007). When the magnetic field perturbations responsible for particle diffusion is self-generated by the CRs, $E_{\rm max}$ is determined by the current in CRs streaming in the upstream medium, $J_{\rm cr}$; such

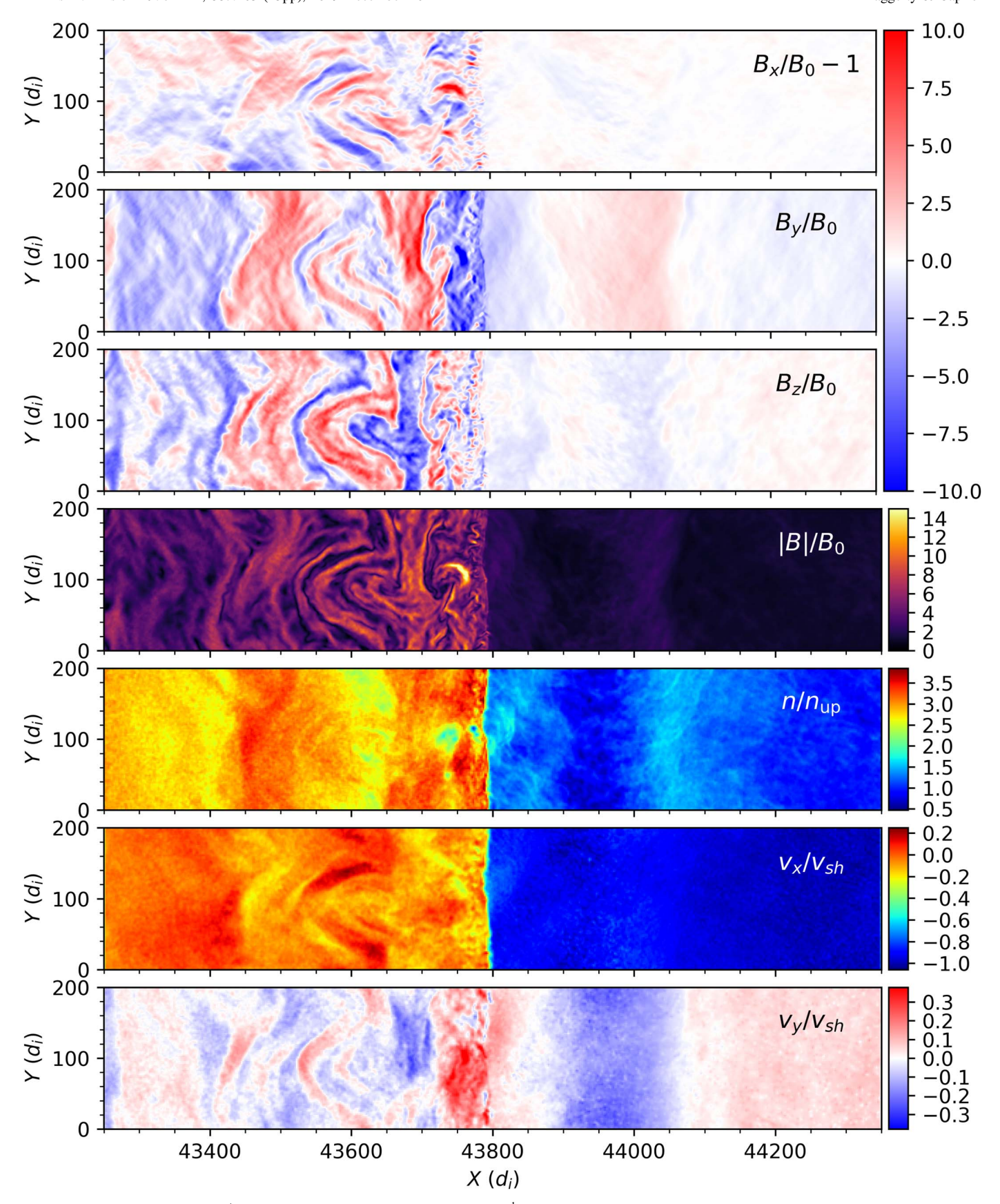


Figure 3. Two-dimensional plasma/fluid quantities around the shock at $t = 5560\Omega_{\rm ci}^{-1}$ from Run A in Table 1. From top to bottom: the three components (x, y and z) of the magnetic field in excess to the background $(B - B_0)$, magnitude of the magnetic field, density, normal (x), and transverse (y) bulk flow. All of the quantities are normalized to the upstream values.

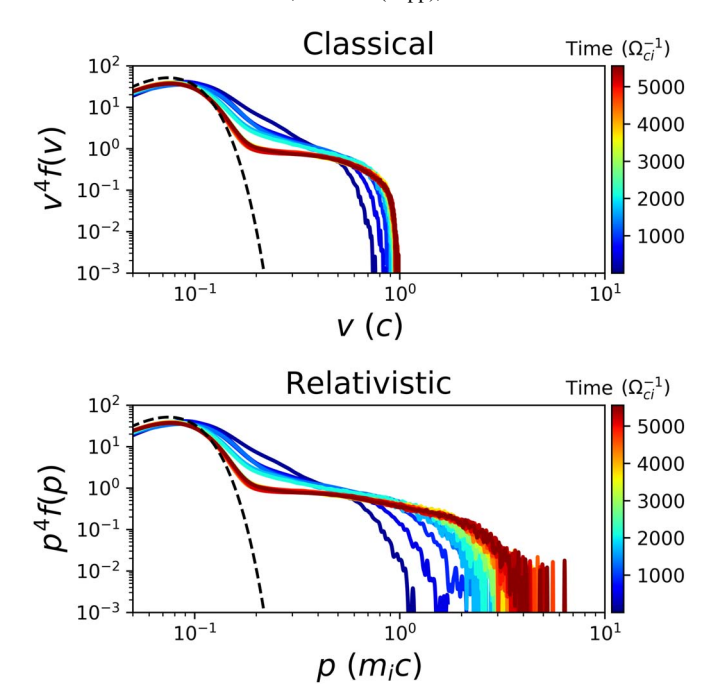


Figure 4. Velocity and momentum spectra calculated downstream of the shock (top and bottom panels) for Run A. Different colors correspond to different times in the simulation, as detailed by the color bars. Velocity and momentum are normalized by c and $m_{\rm ic}$, and spectra are multiplied by v^4 and p^4 for comparison with the standard DSA prediction. The black dashed line shows a Gaussian with temperature $\sim 20\%$ lower than the temperature predicted by the RH conditions, which compensates for the energy that goes into accelerated ions in the power-law tail.

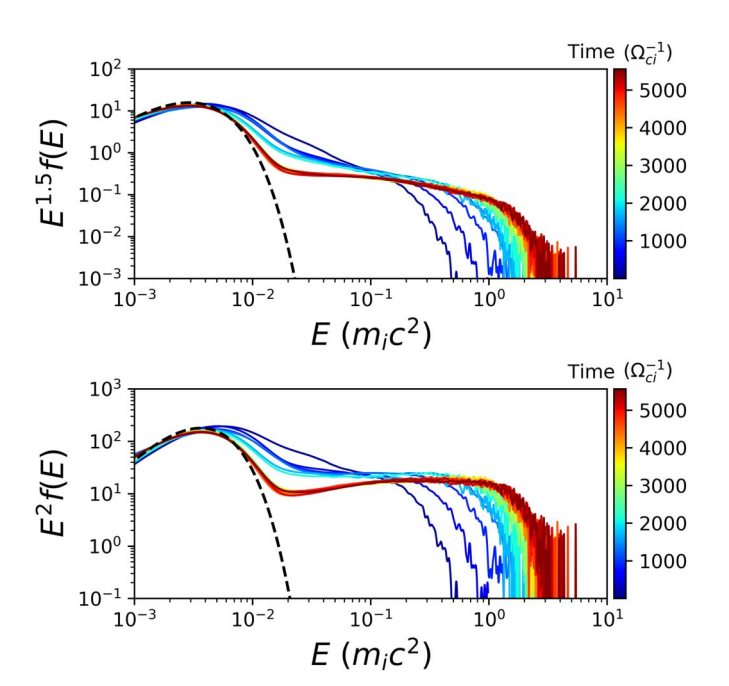
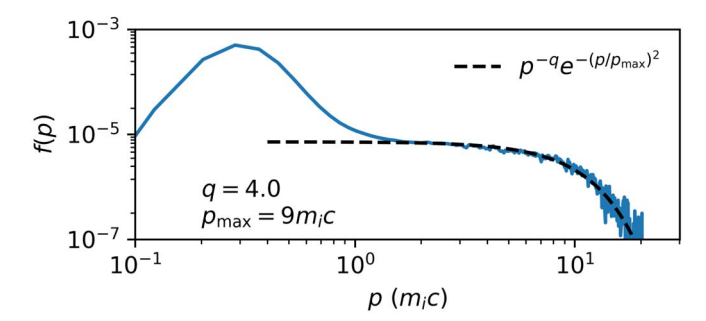


Figure 5. Post-shock spectra as a function of the kinetic energy spectrum normalized to m_{ic}^2 (i.e., $\gamma-1$) for Run A in time. Distributions are multiplied by E^q , where q is the expected power law in the nonrelativistic $(E^{1.5})$ and relativistic (E^2) regimes (top and bottom panels, respectively).

a current can be estimated as the number density $n_{\rm cr}$ of particles close to the instantaneous $E_{\rm max}$, times their velocity, $v_{\rm cr}$. For a momentum spectrum $f(p) \propto p^{-4}$, in the nonrelativistic regime, one has $n_{\rm cr} \propto p_{\rm max}^3 \, f(p) \propto E_{\rm max}^{-1/2}$ and $v_{\rm cr} \propto E_{\rm max}^{1/2}$, so



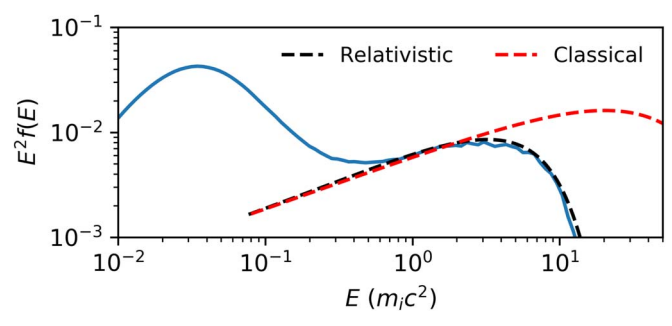


Figure 6. Post-shock momentum and energy distributions in Run B at $t=2000~\Omega_{\rm ci}^{-1}$ (top and bottom panels, respectively). The high-momentum tail is well fit by a distribution $f(p) \propto p^{-q} \exp(-p/p_{\rm max})^2$ with q=4 and $p_{\rm max}=8m_i$ c. Such a fitting curve is converted into an energy fitting using either the classical $(E=p^2/2m_i)$, red line) or the relativistic $(E=m_ic(\sqrt{p^2/c^2+1}-1))$, black line) scalings. The energy distribution is multiplied by E^2 to emphasize the transition from $E^{-1.5}$ to E^{-2} .

 Table 1

 Parameters for the Shock Simulations Presented in This Work

Run	М	$c/V_{\rm A}$	L_x/d_i	$L_{\!\perp}/d_i$	$\Delta x/d_i$	$\Delta t \Omega_{\rm ci}$	$\vartheta_{\mathrm{Bn}}^{\circ}$
A	20	200	8×10^{5}	200	0.5	.0025	0
В	15	50	10^{5}	150	0.5	.005	0
C	30	10000	10^{4}	2700	0.5	.0025	70
3D	5	100	1000	100	0.5	.02	70

Note. From left to right: Alfvénic mach number (i.e., $v_{\rm sh}/V_{\rm A}$), speed of light, longitudinal (L_x) and transverse (L_\perp) box sizes, spacial grid resolution, time step, and angle of the initial magnetic field relative to the upstream plasma bulk flow. Note that the time steps in simulations C and 3D are set by the speed of the fastest particles in the simulation, not by the speed of light.

that $J_{\rm cr} = e n_{\rm cr} v_{\rm cr} \simeq$ is constant in time. Conversely, in the relativistic regime $n_{\rm cr} \propto E_{\rm max}^{-1}$ and $v_{\rm cr} \simeq c$, so that $J_{\rm cr} \propto E_{\rm max}^{-1}$; therefore, the current decreases when the maximum CR energy increases, and one may expect a slower amplification of the magnetic field and in turn a slower rate of increase of $E_{\rm max}$. Note that this effect may be partially compensated for by the fact that the CR precursor becomes larger when $E_{\rm max}$ increases, so that the time available for the growing of the field (on the order of one advection time on a CR diffusion length) also increases. The net effect in general depends on whether most of the field growth is provided by escaping or diffusing particles, and on the details of the instability saturation (Caprioli & Spitkovsky 2014b).

A change in the rate of increase of $E_{\rm max}$ when ions become relativistic was first investigated by Bai et al. (2015) using an MHD-PIC approach. Note that this framework requires specifying a priori the fraction of particles that effectively become CRs, but when acceleration becomes efficient, this

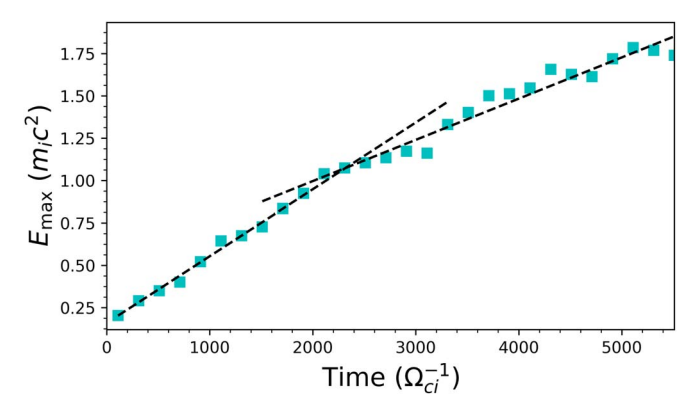


Figure 7. Evolution of the maximum CR energy (Equation (17) in units of $m_i c^2$) for Run A in Table 1.

fraction has to decrease with time to avoid an energy runaway. Because a quantitative theory of how this occurs is still lacking, MHD-PIC methods cannot self-consistently investigate the long-term evolution of the shock.

To quantify the change in the maximum energy, we define $E_{\rm max}$ as the exponential cutoff of the CR distribution, taken in the form $f(E) \sim E^{-q} e^{-E/E_{\rm max}}$. Following Bai et al. (2015), we calculate $E_{\rm max}$ by integrating over the energy distribution function.

$$E_{\text{max}} \sim \frac{\int E^4 f(E) dE}{\int E^3 f(E) dE}.$$
 (17)

Because f(E) has an energy slope between 1.5 and 2, the integral differs from $E_{\rm max}$ by a constant of about unity. Figure 7 shows the maximum energy as a function of time for Run A, where $E_{\rm max}(t) \propto t$ can be fit with a broken linear function with a change of slope in the transrelativistic regime. The rate of the increase of $E_{\rm max}$ is about $3.9 \times 10^{-4} m_i c^2 \Omega_{\rm ci}$ and $2.4 \times 10^{-4} m_i c^2 \Omega_{\rm ci}$ below and above the rest-mass energy, respectively. This decrease by nearly a factor of two is quantitatively consistent with the reduction found in Bai et al. (2015), further supporting the idea that the decrease is due to a reduction in CR current in the relativistic regime.

The connection between the self-generated diffusion and the growth of the maximum CR energy can be made more explicit by measuring the average diffusion coefficient upstream of the shock. For DSA, the return time upstream is typically the bottleneck of the acceleration rate. Such a diffusion coefficient D(E) is estimated using the approach outlined in Caprioli & Spitkovsky (2014c), namely

$$D(E) \simeq \frac{v_{\rm sh}}{f_{\rm sh}(E)} \int_{\rm shock}^{x_0} f(x, E) dx, \tag{18}$$

where x_0 is a position far enough upstream that the CR population is negligible and $f_{\rm sh}(E)$ is the CR distribution function just downstream of the shock.

Figure 8 shows the time evolution of the diffusion coefficient normalized to the Bohm diffusion coefficient ($D_B \equiv vr_L/2$) for Run A. As discussed in Caprioli & Spitkovsky (2014c), for M=20, the diffusion coefficient is about an order of magnitude larger than the Bohm coefficient, which is consistent with having self-generated magnetic fluctuations —at scales resonant with the CRs—that are approximately an order of magnitude smaller

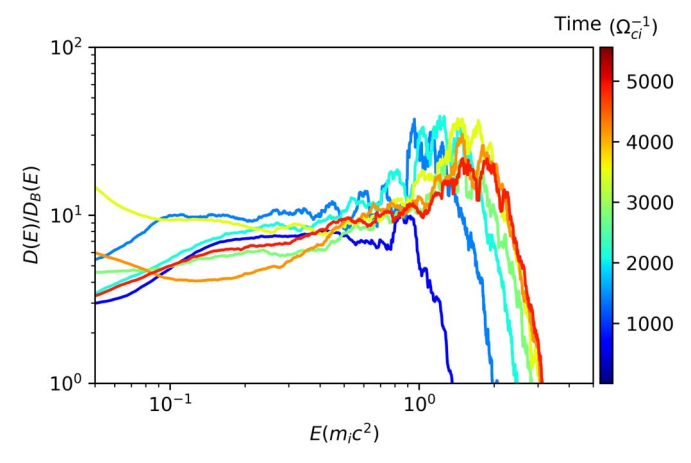


Figure 8. Effective diffusion coefficient (Equation (18)) normalized to the Bohm diffusion coefficient as a function of energy for Run A in Table 1. The different color lines correspond to different times in the simulation.

than the initial upstream magnetic field. As the simulation evolves in time and the maximum energy transitions into the relativistic regime, we can see a change in the diffusion coefficient. We find that the value of the diffusion coefficient is consistently higher at relativistic energies, $D(m_ic^2) \sim 10-20D_B$, than at nonrelativistic energies, $D(m_ic^2/5) \sim 5-10D_B$. The rate of maximum CR energy increase for nonrelativistic shocks can be written as (Caprioli & Spitkovsky 2014c)

$$\frac{E_{\text{max}}(t)}{\frac{1}{2}m_i v_{\text{sh}}^2} \approx \frac{1}{3} \frac{D_B(E_{\text{max}})}{D(E_{\text{max}})} \Omega_{\text{ci}} t.$$
 (19)

The increase in the diffusion coefficient as CRs transition to relativistic energies is consistent with the reduction in the rate of change of E_{max} , as seen in Figure 7. The increase of the diffusion coefficient by an approximate factor of 2 agrees with the reduction of the slope by a comparable factor.

In previous hybrid simulations, the self-generated diffusion coefficient normalized to the Bohm coefficient has been linked to the Mach number by $D/D_B \propto 1/\sqrt{M}$ (Caprioli & Spitkovsky 2014b, 2014c). Using this scaling along with the measured rate of increase of the maximum energy from our simulation, we can calculate a prediction for the maximum energy as a function of time.

$$\frac{E_{\text{max}}}{\text{GeV}} \approx 20 \left(\beta_{\text{sh}}^5 \frac{n}{\text{cm}^{-3}} \frac{B}{\text{Gauss}} \right)^{1/2} \frac{t}{s}, \tag{20}$$

where $\beta_{\rm sh} \equiv v_{\rm sh}/c$. Again, for the typical values of fast radio supernovae, with $\beta_{\rm sh} \gtrsim 0.01$, CRs with GeV energies will be reached within seconds, and TeV CRs will be produced in about an hour. If the circumstellar medium is dense enough, multi-TeV neutrinos¹ in the range of sensitivity of Ice Cube could be produced in a matter of days after the SN explosion.

4.4. Acceleration Efficiency

We consider the evolution of the fraction of shock energy that is transferred to CRs as a function of time. Following Caprioli & Spitkovsky (2014a) and Caprioli et al. (2015), we

 $^{^1}$ Hadronic neutrinos and $\gamma\text{-rays}$ of energy E are produced by parent protons of energy $\sim\!10E$.

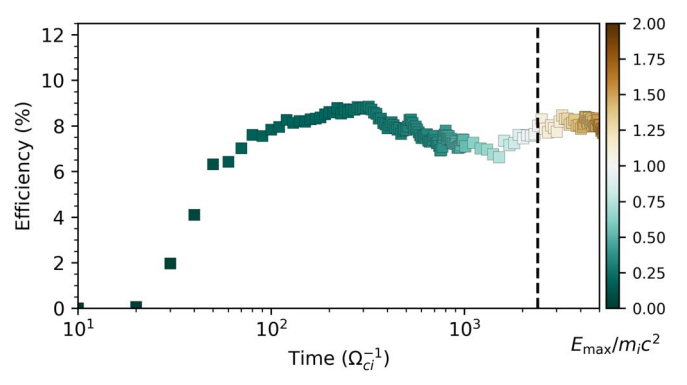


Figure 9. CR acceleration efficiency (fraction of energy in particles with $E>10E_{\rm sh}$) as a function of time for Run A. The black dashed vertical line corresponds to the time when the highest energy particles become relativistic. The color of each point corresponds to $E_{\rm max}/m_ic^2$, as shown in Figure 7.

distinguish the CRs as the ions that achieved energies $E \gtrsim 10E_{\rm sh}$ and define the acceleration efficiency $\varepsilon_{\rm cr}$ as the fraction of the energy density in these particles normalized by the total energy density,

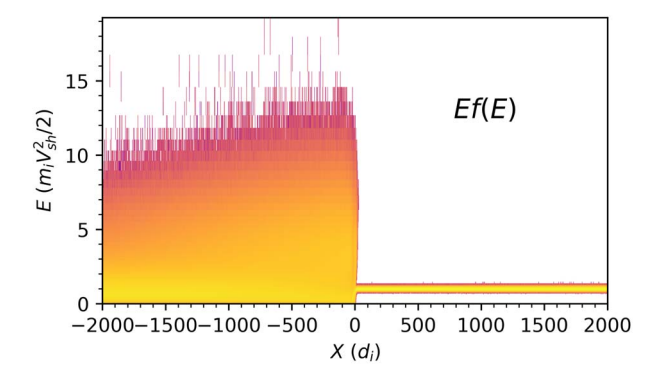
$$\varepsilon_{cr} = \frac{\int_{10E_{\rm sh}}^{\infty} Ef(E)dE}{\int_{0}^{\infty} Ef(E)dE}.$$
 (21)

Figure 9 shows that an acceleration efficiency on the order of 10% is reached within the first hundred inverse cyclotron times, and then remains nearly constant throughout the entire simulation, consistent with what was seen in the nonrelativistic case (Caprioli & Spitkovsky 2014a). The vertical black dashed line denotes when $E_{\rm max} \sim m_i c^2$, and the color corresponds to $E_{\rm max}/m_i c^2$ as shown in Figure 7.

From this it is clear that $\varepsilon_{\rm cr}$ is unaffected as the CR population transitions from nonrelativistic to relativistic energies, and that the canonical value of $\sim 10\%$ quoted by Caprioli & Spitkovsky (2014a) should be considered the asymptotic value. In this respect, it is worth stressing that in the nonrelativistic regime the efficiency $\varepsilon_{\rm cr} \propto E^2 f(E) \propto E^{1/2}$ is typically dominated by the highest energy CRs, while in the relativistic regime there is about the same energy density per decade. Because $\varepsilon_{\rm cr}$ saturates well before CRs become transrelativistic, it is necessary for the shock to "be aware" of the efficient CR acceleration; this CR feedback will be discussed in greater detail in forthcoming works, but here we mention that the pressure in the CR precursor affects the dynamics shock front, which reacts by injecting fewer particles into the DSA.

Until this moment, we have not discussed oblique or perpendicular shocks. This is because it has previously been found in classical hybrid simulations that shocks with $\vartheta_{\rm Bn}\gtrsim 50^{\circ}$, thermal ions are not energized enough to initiate the DSA process (Caprioli & Spitkovsky 2014a; Caprioli et al. 2015). Note that if the injection issue is overcome, for instance, when preenergized CR seeds are present (Caprioli et al. 2018), or the presence of external plasma turbulence, acceleration at oblique shocks proceeds unhindered, even more rapidly than at quasi-parallel shocks (e.g., Jokipii 1987; Giacalone 2005)

Recently, PIC-MHD simulations of very oblique shocks $(\vartheta_{Bn} \gtrsim 70^{\circ})$ have suggested that thermal particle injection and DSA will eventually occur for simulations that are run long enough (van Marle et al. 2018). We have tested this claim with the



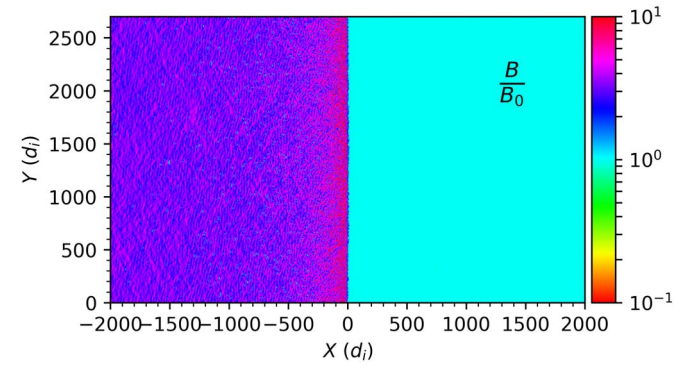


Figure 10. Quantities from the quasi-perpendicular shock simulation described by Run C in Table 1. Top panel: energy spectrum at each position *x*. Bottom panel: 2D plot of the magnitude of the magnetic field. There is no evidence of DSA and of magnetic field amplification upstream.

full-hybrid dHybridR code and did not recover such a result. Figure 10 shows a simulation perform with the same initial parameters as the quasi-perpendicular M = 30 simulation discussed in van Marle et al. (2018). The simulation is $[L_x; L_{\perp}] = [10^4; 2.7 \times 10^3] d_{i0}$ in size with two cells per skin depth in each direction and was run for a comparable amount of time (600 Ω_{ci}^{-1}). Using four particles per cell, the dHybridR simulation has approximately $4/3 \times M \times 16 \times 2700 \simeq 1.72 \times 10^{-2}$ 10⁶ macroparticles impinging on the shock per unit cyclotron time, where the factor of $r/(r-1) \simeq 4/3$ comes from the conversion of the upstream flow speed from the simulation to the shock frame. For the canonical 1% injection efficiency (Caprioli et al. 2015), in our simulation $\sim 1.7 \times 10^4$ CR particles are produced per unit time, which returns a statistics comparable with the $\sim 10^4$ rate used by van Marle et al. (2018). The top panel shows the energy density distribution as a function of x, in which energy is normalized to the shock energy. Downstream of the shock (x < 0), ions are heated up to suprathermal energies $(E \lesssim 10E_{\rm sh})$, but there is no DSA tail, and no energetic particles are found upstream (x > 0). The bottom panel of Figure 10 shows a 2D plot of the magnitude of the magnetic field, which reveals the canonical downstream compression, with some additional small-scale deviations (which we discuss below); the upstream magnetic field, instead, is unperturbed. These results stress that a self-consistent model for ion injection can only be provided by full-hybrid simulations.

5. 3D Simulations

Finally, we present a quasi-perpendicular 3D shock simulation with a smaller Mach number (M = 5), identified as Run 3D in Table 1. The conditions in this simulation are quite similar to

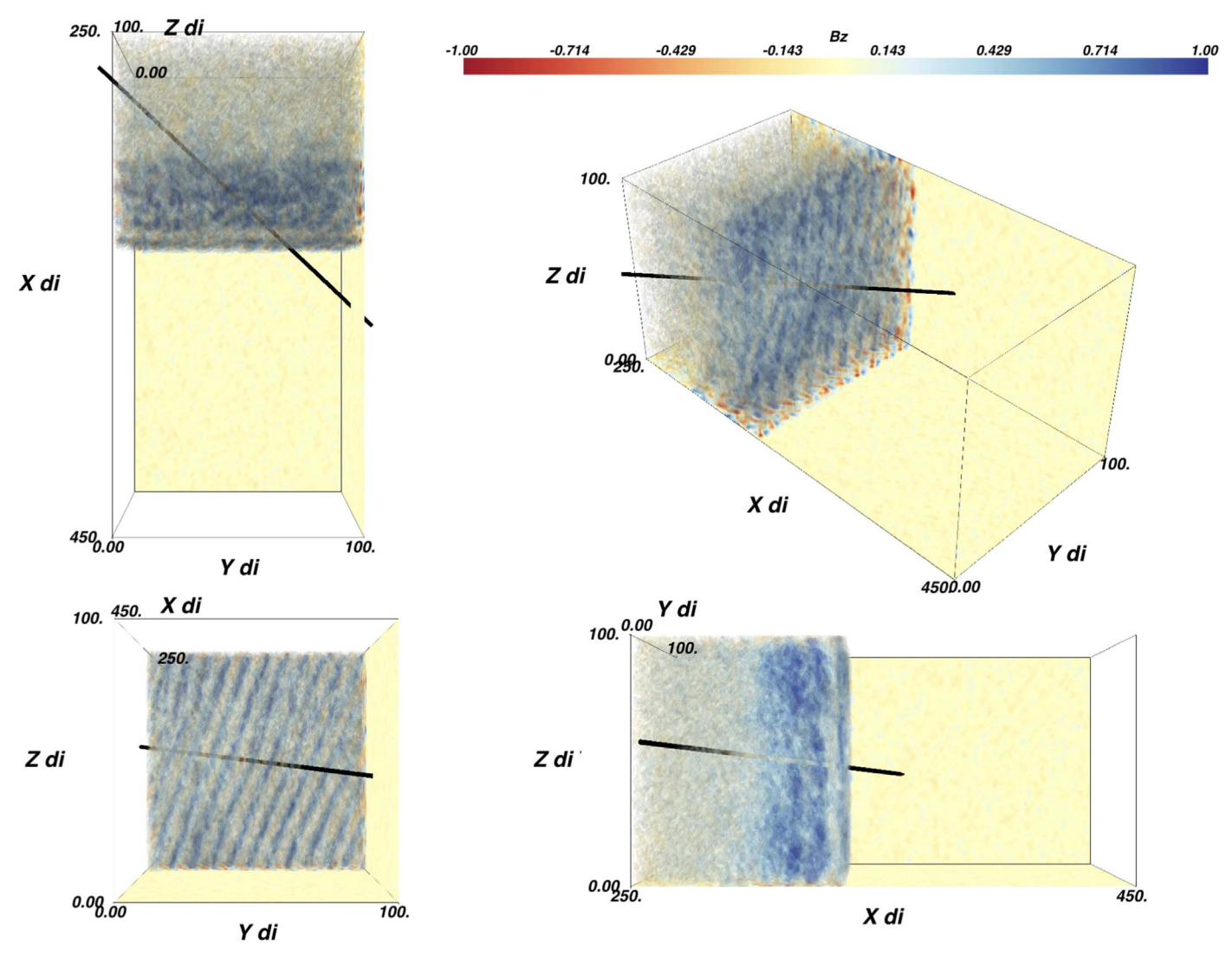


Figure 11. Orthographic projection of B_z (self-generated component normal to the upstream flow and mean magnetic field) around the shock from Run 3D. Four views of the 3D structure, with the following views from bottom right in clockwise order: viewing along $+\hat{y}$, along $-\hat{x}$, along $-\hat{x}$, and an isometric view along $(-\hat{x} + \hat{y} - \hat{z})/\sqrt{3}$. Slices of B_z in the x, y and x, z direction are plotted along the edge of the plotting domain. The black line represents the trajectory of the 1D cut shown in Figure 12.

typical heliospheric shocks, such as the Earth's bow shock, which is formed by the supersonic/super-Alfvénic solar wind, traveling at speed $\gtrsim 100 \,\mathrm{km \, s^{-1}}$ and impinging on the Earth's magnetosphere (Sheeley et al. 1985; Cane & Richardson 2003). For typical solar wind conditions, the ion temperature is about 10 eV, and thermal and magnetic pressure are comparable to each other, which corresponds to $M \approx 5-10$ (e.g., Schwartz et al. 1988; Wilson et al. 2018); moreover, interplanetary shocks triggered by coronal mass ejections typically span the same range of Mach numbers (e.g., Wilson et al. 2019). dHybridR is well suited to study low-Mach-number heliospheric shocks because in this system, ions can be accelerated to transrelativistic energies and because the relevant sizes and scales can be modeled to scale at a reasonable computational cost. In Figure 11 we present an orthographic projection of B_z , where z is the direction normal to the upstream flow and the mean upstream magnetic field; therefore, B_7 is the selfgenerated component of the magnetic field. Upstream of the shock there are no indications of magnetic field amplification, in agreement with the 2D simulation. However, downstream,

some magnetic structures can be observed: there is a clear rippling of the magnetic field along the shock interface, which is produced by shock reformation, consistent with what has previously been found in observations (Johlander et al. 2016, 2018) and simulations (Lowe & Burgess 2003; Caprioli et al. 2015; Burgess et al. 2016).

The black line in Figure 11 represents the trajectory of a synthetic probe through the simulation box, mimicking in situ spacecraft observations, and Figure 12 shows the magnetic field measured by such a probe. The trajectory is diagonal through the shock interface, with only a small component normal to the upstream magnetic field $(0.681\hat{x} + 0.727\hat{y} - 0.091\hat{z})$ intersecting a point in the middle of the y-z plane at $x = 312.5d_i$). From this cut, the periodic structure of the ripples can be clearly seen; considering that the direction of propagation is primarily in the y direction, the wave number can be estimated to be on the order of $k\Omega_{ci}/v_{sh} \sim kr_g \sim 1$, where r_g is the gyroradius of the downstream population. This is a great example of how dHybridR simulations can be directly compared with in situ measured heliospheric plasma phenomena.

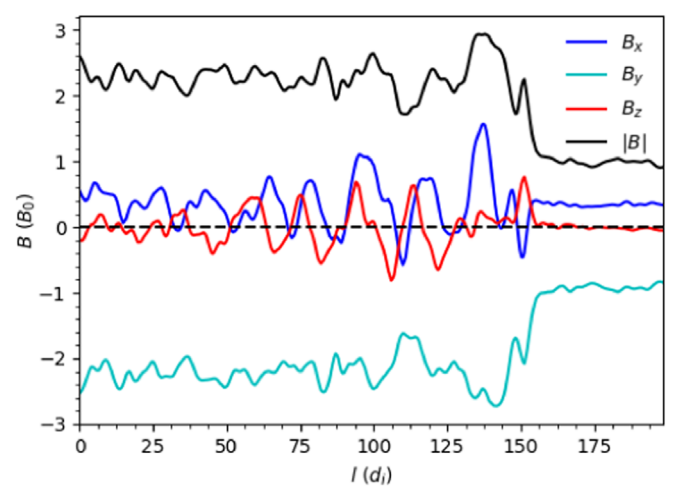


Figure 12. Three components and magnitude of the magnetic field along an oblique trajectory across the shock (from Run 3D Table 1). The trajectory is denoted by the black line in 3D projection view in Figure 11.

6. Conclusion

In this work we presented the first results from dHybridR, a hybrid plasma simulation code that includes relativistic ion dynamics. We detailed how relativistic ion motion is included in the code and how for specific systems of interest, the assumptions required for hybrid simulations are not violated. This novel simulation software can be used to help understand, from first principles, numerous different open problems involving space and astrophysical plasmas. The code is well suited to study many astrophysical systems where a high-energy, low-density CR population interacts with a nonrelativistic thermal background population.

To verify that dHybridR can correctly model physical systems of interest, we simulated CR-driven nonresonant and resonant streaming instabilities. In both test cases, the location in k space and the value of the maximum growth rate found in simulations agreed remarkably well with the linear prediction. Then, we moved to use dHybridR to model strongly nonlinear problems such as DSA at nonrelativistic collisionless shocks, similar to those found in the heliosphere, in SN remnants, and in galaxy clusters. In particular, we presented simulations with parameters relevant to fast SN shocks (radio SNe, Figure 3) as well as heliospheric shocks, such as the Earth's bow shock (Figure 11).

We performed unprecedentedly long simulations of parallel shocks in which ions achieve Lorentz factors as large as $\gamma \gtrsim 20$, attesting for the first time in hybrid simulations that DSA produces a power-law tail in momentum across the transrelativistic regime, which implies an energy distribution that follows a broken power law that steepens by 0.5 in slope. When CRs become relativistic, the increase of the maximum particle energy is still linear in time, but with a rate reduced by a factor of \sim 2; this reduction is a consequence of the saturation of the velocity of escaping particles to c.

The acceleration efficiency (i.e., the fraction of the shock energy channeled into nonthermal particles with energy $E\gtrsim 10E_{\rm sh}$) was found to reach about 10% within tens of cyclotron times and to remain nearly constant as the high-energy population transitions into the relativistic regime. These results are directly applicable to fast radio SNe, where we predict GeV/TeV CRs to be produced within seconds/days.

With the current sensitivity of γ -ray and neutrino telescopes, this delay could be measured for a Galactic SN.

Finally, we presented a 3D simulation produced with dHybridR with conditions comparable to the Earth's bow shock with a quasi-perpendicular configuration. We showed that dHybridR reproduces both qualitatively and quantitatively the shock rippling that has been found with in situ satellite observations (Johlander et al. 2018).

In summary, this work presents, to the authors' knowledge, the first hybrid simulations to include relativistic ion dynamics, which is a critical tool for studying the inherently multiscale nature of CR/thermal ion interplay in space and astrophysical plasmas.

We would like to thank Luis Gargaté for providing the original version of dHybrid. This research was partially supported by NASA (grant NNX17AG30G, 80NSSC18K1218, and 80NSSC18K1726) and NSF (grants AST-1714658 and AST-1909778). Simulations were performed on computational resources provided by the University of Chicago Research Computing Center, the NASA High-End Computing Program through the NASA Advanced Supercomputing Division at Ames Research Center, and XSEDE TACC (TG-AST180008).

ORCID iDs

Colby C. Haggerty https://orcid.org/0000-0002-2160-7288 Damiano Caprioli https://orcid.org/0000-0003-0939-8775

References

```
Amato, E., & Blasi, P. 2009, MNRAS, 392, 1591
Arzamasskiy, L., Kunz, M. W., Chandran, B. D. G., & Quataert, E. 2019, ApJ,
  879, 53
Axford, W. I., Leer, E., & Skadron, G. 1977, Proc. ICRC, 2, 273
Baade, W., & Zwicky, F. 1934, PNAS, 20, 259
Bai, X.-N., Caprioli, D., Sironi, L., & Spitkovsky, A. 2015, ApJ, 809, 55
Bai, X.-N., Ostriker, E. C., Plotnikov, I., & Stone, J. M. 2019, ApJ, 876, 60
Bell, A. R. 1978a, MNRAS, 182, 147
Bell, A. R. 1978b, MNRAS, 182, 443
Bell, A. R. 2004, MNRAS, 353, 550
Bell, A. R., Robinson, A. P. L., Sherlock, M., Kingham, R. J., & Rozmus, W.
  2006, PPCF, 48, R37
Birdsall, C. K., & Langdon, A. B. 1991, Plasma Physics via Computer
  Simulation (Boca Raton, FL: CRC Press)
Blandford, R. D., & Ostriker, J. P. 1978, ApJL, 221, L29
Blasi, P., Amato, E., & Caprioli, D. 2007, MNRAS, 375, 1471
Burgess, D. 1989, GeoRL, 16, 163
Burgess, D., Hellinger, P., Gingell, I., & Travnicek, P. M. 2016, JPIPh, 82,
  905820401
Burgess, D., Möbius, E., & Scholer, M. 2012, SSRv, 173, 5
Burgess, D., & Scholer, M. 2013, SSRv, 178, 513
Cane, H. V., & Richardson, I. G. 2003, JGRA, 108, 1156
Caprioli, D. 2015, Proc. ICRC, 34, 8
Caprioli, D., & Haggerty, C. 2019, Proc. ICRC, 36, 209
Caprioli, D., Pop, A., & Spitkovsky, A. 2015, ApJL, 798, L28
Caprioli, D., & Spitkovsky, A. 2014a, ApJ, 783, 91
Caprioli, D., & Spitkovsky, A. 2014b, ApJ, 794, 46
Caprioli, D., & Spitkovsky, A. 2014c, ApJ, 794, 47
Caprioli, D., Yi, D. T., & Spitkovsky, A. 2017, PhRvL, 119, 171101
Caprioli, D., Zhang, H., & Spitkovsky, A. 2018, JPIPh, 84, 715840301
Chen, G., & Armstrong, T. P. 1975, Proc. ICRC, 5, 1814
Chevalier, R. A., & Fransson, C. 2006, ApJ, 651, 381
Crumley, P., Caprioli, D., Markoff, S., & Spitkovsky, A. 2019, MNRAS,
  485, 5105
Desai, M. I., Mason, G. M., Dayeh, M. A., et al. 2016, ApJ, 816, 68
Dubois, Y., Commerçon, B., Marcowith, A. r., & Brahimi, L. 2019, A&A,
  631, 121
Fermi, E. 1949, PhRv, 75, 1169
```

```
Gargaté, L., Bingham, R., Fonseca, R. A., & Silva, L. O. 2007, CoPhC,
   176, 419
Gargaté, L., Fonseca, R. A., Niemiec, J., et al. 2010, ApJL, 711, L127
Gargaté, L., & Spitkovsky, A. 2012, ApJ, 744, 67
Giacalone, J. 2004, ApJ, 609, 452
Giacalone, J. 2005, ApJL, 628, L37
Giacalone, J., Burgess, D., Schwartz, S. J., & Ellison, D. C. 1992, GeoRL,
   19.433
Giacalone, J., Burgess, D., Schwartz, S. J., Ellison, D. C., & Bennett, L. 1997,
   JGR, 102, 19789
Haggerty, C., Caprioli, D., & Zweibel, E. 2019, Proc. ICRC, 36, 279
Hockney, R., & Eastwood, J. 1988, Computer Simulation Using Particles
   (Bristol: Hilger)
Holcomb, C., & Spitkovsky, A. 2019, ApJ, 882, 3
Johlander, A., Schwartz, S. J., Vaivads, A., et al. 2016, PhRvL, 117, 165101
Johlander, A., Vaivads, A., Khotyaintsev, Y. V., et al. 2018, PPCF, 60, 125006
Jokipii, J. R. 1987, ApJ, 313, 842
Karimabadi, H., Roytershteyn, V., Vu, H. X., et al. 2014, PhPl, 21, 062308
Krall, N., & Trivelpiece, A. 1973, Principles of plasma physics, International
   Series in Pure and Applied Physics No. v. 0-911351 (New York:
   McGraw-Hill)
Krymskii, G. F. 1977, DoSSR, 234, 1306
Kulsrud, R. M., & Cesarsky, C. J. 1971, ApJ, 8, 189
Kulsrud, R., & Pearce, W. P. 1969, ApJ, 156, 445
Lagage, P. O., & Cesarsky, C. J. 1983, A&A, 118, 223
Lapenta, G. 2012, JCoPh, 231, 795
Le, A., Egedal, J., Daughton, W., Fox, W., & Katz, N. 2009, PhRvL, 102,
   085001
Lipatov, A. S. 2002, The Hybrid Multiscale Simulation Technology: An
   Introduction with Application to Astrophysical and Laboratory Plasmas
   (Berlin; New York: Springer)
Lowe, R. E., & Burgess, D. 2003, AnGeo, 21, 671
```

Lucek, S. G., & Bell, A. R. 2000, MNRAS, 314, 65

Mandt, M. E., Denton, R. E., & Drake, J. F. 1994, GeoRL, 21, 73

```
Matthaeus, W. H., Wan, M., Servidio, S., et al. 2015, RSPTA, 373, 20140154
Mignone, A., Bodo, G., Vaidya, B., & Mattia, G. 2018, ApJ, 859, 13
O'C. Drury, L. 1983, RPPh, 46, 973
Ohira, Y., Reville, B., Kirk, J. G., & Takahara, F. 2009, ApJ, 698, 445
Palmroth, M., Ganse, U., Pfau-Kempf, Y., et al. 2018, LRCA, 4, 1
Park, J., Caprioli, D., & Spitkovsky, A. 2015, PhRvL, 114, 085003
Pecora, F., Servidio, S., Greco, A., et al. 2018, JPIPh, 84, 725840601
Quest, K. B. 1988, JGR, 93, 9649
Reames, D. V. 1999, SSRv, 90, 413
Reames, D. V. 2013, SSRv, 175, 53
Riquelme, M. A., & Spitkovsky, A. 2009, ApJ, 694, 626
Schwartz, S. J., Thomsen, M. F., Bame, S. J., & Stansberry, J. 1988, JGR, 93,
Shay, M. A., Drake, J. F., Rogers, B. N., & Denton, R. E. 2001, JGR,
  106, 3759
Sheeley, N. R. J., Howard, R. A., Michels, D. J., et al. 1985, JGR, 90, 163
Skilling, J. 1975, MNRAS, 172, 557
Tylka, A. J., Cohen, C. M. S., Dietrich, W. F., et al. 2005, ApJ, 625, 474
Valentini, F., Trávníček, P., Califano, F., Hellinger, P., & Mangeney, A. 2007,
  JCoPh, 225, 753
van Marle, A. J., Casse, F., & Marcowith, A. 2018, MNRAS, 473, 3394
Weidl, M. S., Winske, D., & Niemann, C. 2019, ApJ, 872, 48
Weidl, M. S., Winske, D., & Niemann, C. 2019, ApJ, 873, 57
Wilson, L. B., III, Sibeck, D. G., Turner, D. L., et al. 2016, PhRvL, 117,
  215101
Wilson, L. B., III, Chen, L.-J., Wang, S., et al. 2019, ApJS, 243, 8
Wilson, L. B., III, Stevens, M. L., Kasper, J. C., et al. 2018, ApJS, 236, 41
Winske, D. 1985, SSRv, 42, 53
Winske, D., & Omidi, N. 1996, JGR, 101, 17287
Yoast-Hull, T. M., Gallagher, J. S., III, Zweibel, E. G., & Everett, J. E. 2014,
     J, 780, 137
Zacharegkas, G., Caprioli, D., & Haggerty, C. 2019, Proc. ICRC, 36, 483
Zachary, A. L., & Cohen, B. I. 1986, JCoPh, 66, 469
Zweibel, E. G. 2003, ApJ, 587, 625
```